Dihydroalterperylenol from endophytic fungus *Alternaria semiverrucosa* and its antitumour activity uncovered by transcriptome analysis, molecular docking and molecular dynamics simulations

MINGFEI YANG[1-3], YONGZHONG LU[4], LONG HAN[1,2], ZHANGJIANG HE[2] and JICHUAN KANG[2]

[1]College of Life Sciences, Guizhou University, Guiyang, Guizhou 550025, P.R. China; [2]Engineering Research Center for Utilization of Characteristic Bio-Pharmaceutical Resources in Southwest China, Ministry of Education, Guizhou University, Guiyang, Guizhou 550025, P.R. China; [3]School of Public Health, Guiyang Healthcare Vocational University, Guiyang 550081, Guizhou, P.R. China; [4]School of Food and Pharmaceutical Engineering, Guizhou Institute of Technology, Guiyang, Guizhou 550003, P.R. China

Received March 2, 2025; Accepted August 5, 2025

DOI: 10.3892/mmr.2025.13740

Abstract. Medicinal plants host a variety of endophytic fungi, which produce numerous secondary metabolites with diverse biological activities. The present study identified ten natural compounds isolated from the endophytic fungal strain *Alternaria semiverrucosa*, derived from *Taxus wallichiana* var. *mairei*. The cytotoxicity of all isolated compounds was evaluated against six tumor cell lines. Dihydroalterperylenol (compound 1) exhibited the highest cytotoxicity against HeLa cells (IC_{50}=6.43±3.0 μM). Cells were treated with 0.1% DMSO and 6.0 μmol/l for 24 h, after which total RNA was extracted for transcriptome library construction and sequencing analysis. Transcriptome analysis identified 140 differentially expressed genes (DEGs), including 99 upregulated and 41 downregulated genes. Kyoto Encyclopedia of Genes and Genomes pathway analysis revealed significant enrichment of these DEGs in the TGFβ signaling pathway and Hippo signaling pathway. Gene ontology analysis indicated that the DEGs were predominantly involved in the regulation of cell proliferation. Notably, reverse transcription-quantitative PCR validation confirmed the upregulation of three genes (TGIF2, ID1 and BMP2) which was consistent with the transcriptome sequencing results. Additionally, molecular docking and molecular dynamics simulations were employed to explore the molecular mechanisms underlying the antitumor activity of compound 1. The results suggest that compound 1 exerts its anticancer effects in cervical cancer by regulating the expression of genes TGIF2, ID1 and BMP2.

Correspondence to: Professor Jichuan Kang, Engineering Research Center for Utilization of Characteristic Bio-Pharmaceutical Resources in Southwest China, Ministry of Education, Guizhou University, 24 Xiahui Road, Huaxi, Guiyang, Guizhou 550025, P.R. China
E-mail: jckang@gzu.edu.cn

Key words: *Alternaria semiverrucosa*, cervical cancer cells, dihydroalterperylenol, inhibition of proliferation, transcriptome analysis, molecular docking, molecular dynamics simulations

Introduction

Cervical cancer is one of the most common types of gynecological cancer and ranks as the fourth leading cause of cancer-related mortality among women, and 14th overall among all types of cancer (1,2). According to the GLOBOCAN 2022 report, ~660,000 new cases of cervical cancer were diagnosed, with ~340,000 mortalities attributed to the disease (3). Extensive evidence suggests that cervical cancer is primarily caused by human papillomavirus infection, with additional contributing factors associated with social factors (such as income, education and region) and individual behaviors (such as age, sex, smoking status, nutrition, activity level) (4,5). This is exemplified by the obvious regional differences in the incidence and mortality of cervical cancer within China. Surveillance data from the Chinese cancer registry shows that incidence and mortality rates in rural areas are consistently higher than those in urban areas. This disparity is attributed to inequalities in health education, access to HPV screening, and availability of vaccination programs. Furthermore, it is estimated that among younger women, this gap in incidence rates between urban and rural populations is likely to widen further, highlighting the critical role of socioeconomic factors in disease outcomes (4). Excessive cell division and proliferation are central to the development of cervical cancer (6,7), making the inhibition of cancer cell proliferation and the induction of apoptosis key therapeutic strategies.

Endophytic fungi, which reside within the tissues of medicinal plants and co-evolve with their hosts (8), produce a diverse array of natural products (9,10). These products exhibit a range of biological activities, including antioxidant, anti-inflammatory, antibacterial, antiviral and anticancer properties (11). Anti-tumor natural products have been

classified into several structural groups, such as alkaloids (12), terpenoids (13), steroids (14), quinones (15) and esters (10).

Taxus wallichiana var. *mairei*, a rare and endangered plant native to southern China, is well-known for producing the anti-cancer drug paclitaxel (16). Fungal endophytes isolated from *Taxus wallichiana* var. *mairei* include species such as *Phoma medicaginis* (17), *Diaporthe phaseolorum* (18) and *Nigrospora oryzae* (19). The genus *Alternaria* (family Dematiaceae) consists of globally distributed filamentous fungi and plant pathogens (20,21), known for producing a variety of secondary metabolites (22).

Dihydroalterperylenol (DAP) is a perylenequinone metabolite characterized by a highly conjugated pentacyclic core. A previous study has reported that DAP does not exhibit cytotoxicity (23). The present study demonstrated the potent cytotoxic activity of DAP isolated from the plant endophytic fungus *Alternaria semiverrucosa* in HeLa cells and explored its apoptosis-inducing mechanism through transcriptome analysis, molecular docking and molecular dynamics (MD) simulations studies.

Materials and methods

Materials and instruments for chemical separation. Silica gel (200-300 mesh; Qingdao Haiyang Chemical Co. Ltd.), Sephadex LH-20 gel (Shanghai Yuanye Bio-Technology Co. Ltd.), Octadecylsilyl-bonded (ODS) silica gel (cat. no. RP-18; Merck KGaA) and organic solvents (methanol, CAS No: 67-56-1; dichloromethane, CAS No: 75-09-2; petroleum ether, CAS No: 8032-32-4; ethyl acetate, CAS No: 141-78-6; All the aforementioned reagents are analytical grade; Tianjin Fuyu Fine Chemical Co. Ltd.) were used for column chromatography. Thin-layer chromatography was monitored using silica gel plates (type H; Qingdao Dingkang Silicone Co. Ltd.). One-dimensional nuclear magnetic resonance (NMR) spectra were recorded using Bruker Avance-500 and 600 spectrometers (Beijing Obel Scientific Instrument Co., Ltd.).

Fungal material and fermentation. All specimens of *Taxus chinensis* var. *mairei* were obtained through artificial propagation and exclusively sourced from the Wanshun Seedling Farm Guiyang, China. Voucher specimens of the host plant have been deposited at the Engineering Research Center for Utilization of Characteristic Bio-Pharmaceutical Resources in Southwest China, Ministry of Education, Guizhou University, with the accession number ZZ-HJ-13. The endophytic fungus *Alternaria semiverrucosa* was isolated from the healthy branches of *Taxus chinensis* var. *mairei*. The fungal isolate *Alternaria semiverrucosa* was preserved at the Guizhou Academy of Agricultural Sciences under strain code (dried culture; holotype no. GZAAS 22-2029; ex-type living culture, no. GZCC 22-2029). The fungus was cultured on potato dextrose agar plates for 10 days. The mycelia were then sliced and incubated in 300 ml Yeast extract-Peptone-Starch (YPS) medium (glucose 20.0 g, peptone 10.0 g, yeast extract 5.0 g, KH_2PO_4 1.0 g, $MgSO_4$ 1.0 g and 1 l distilled water) for 3 days at 28˚C. A 15 ml aliquot of the seed culture was transferred to 400 x 1 l Erlenmeyer flasks, each containing 300 ml of YPS culture medium. The flasks were shaken on a rotary shaker (140 rpm) at 28˚C for 3 days, followed by static cultivation for 30 days.

Extraction and isolation. After cultivation, the broth and mycelia were separated by gauze. The broth was extracted with ethyl acetate (EtOAc) three times. The EtOAc extract was collected and concentrated under vacuum to yield 120.0 g of extract, while the mycelia were extracted with methanol to obtain a 250.0 g extract after evaporation under reduced pressure. Both the EtOAc and methanol extracts were subjected to silica gel column chromatography with a step gradient of CH_2Cl_2-MeOH (1:0 → 0:1 v/v), yielding 28 fractions (Fr.1-Fr.28) from the EtOAc extract and 22 fractions (Fr.A-Fr.V) from the methanol extract. Fr.11 was separated on an ODS column, eluting with a CH_3OH/H_2O gradient, yielding five subfractions (Fr.11.1-Fr.11.5). Fr.11.2 was further purified using a silica gel column, resulting in compound 1 (11.9 mg). Fr.11.3 was purified by Sephadex LH-20 and silica gel column chromatography to yield compound 4 (27.9 mg). Fr.16 was separated on an ODS column, eluted with a methanol-water gradient (10-100%), yielding six subfractions (Fr.16.1-Fr.16.6). Fr.16.3 was further purified on silica gel and Sephadex LH-20 to obtain compound 2 (9.8 mg) and Fr.16.6 was chromatographed on an ODS column to yield compound 3 (7.2 mg). Fr.13 was purified by ODS column chromatography, followed by repeated silica gel column purification, yielding compounds 5 (27.9 mg) and 6 (18.4 mg). Compound 7 (21.8 mg) was obtained by repeated Sephadex LH-20 and silica gel column chromatography. Fr.8 was separated on an RP-C18 column using a methanol-water gradient to yield six subfractions (Fr.8.1-Fr.8.6). Fr.8.1 was purified by repeated Sephadex LH-20 chromatography to yield compound 8 (18.9 mg). Fr.I was separated by RP-C18 column chromatography with a methanol-water gradient (20-80%), yielding five subfractions (Fr.I.1-Fr.I.5). Fr.I.2 was further purified by Sephadex LH-20, resulting in compound 9 (18.8 mg). Fr.I.3 was purified by silica gel column chromatography to yield compound 10 (31.5 mg).

Cell culture and cytotoxicity assay. A total of six human cancer cell lines (PC3 cat. no. CRL-1435; LNCaP, cat. no. CRL-1740; HeLa, cat. no. CCL-2; SiHa, cat. no. HTB-35; K562, cat. no. CCL-243; and HEL, cat. no. TIB-180) were purchased from Typical Cultures Depository of the United States of America and are currently maintained in the Key Laboratory of Chemistry for Natural Products of Guizhou, Chinese Academy of Sciences in Guiyang, China. Human gingival fibroblasts (HGF-1) were provided by Guiyang Stomatological Hospital in Guiyang, China. The inhibitory effects of the compounds on tumor cells were assessed using the MTT assay, as described in a previous study (24). A volume of 20 μl 5 mg/ml 3-(4,5-dimethylthiazolyl-2)-2,5-diphenyltetrazolium bromide (MTT; M158055, Aladdin) solution was added to each well and incubated for 4 h at 37˚C. After centrifugation at 20 x g for 10 min at room temperature to remove the supernatant, 150 μl DMSO was added, followed by shaking on a shaker for 15 min. Absorbance at 490 nm was measured using a microplate reader to calculate the cell proliferation inhibition rate. Inhibition rate of the proliferation=1-(Average optical density of experimental group/Average optical density of control group) x100%. The cells were cultured in RPMI

1640 medium (cat. no. A-CSH807-500ml; Biogradetech, Inc.) supplemented with 10% fetal bovine serum (cat. no. C0230; Beyotime Institute of Biotechnology) and 1% penicillin-streptomycin solution, in an incubator for 24 h at 37˚C under 5% CO_2 atmosphere. Cell viability was calculated as a percentage relative to control wells. The half-maximal inhibitory concentration (IC_{50}) values were determined using MTT viability curves, and the data were analyzed with GraphPad Prism 8.0 (Dotmatics). Doxorubicin (cat. no. D1515; Merck KGaA) was used as a positive control and was applied at concentrations of 0.0, 0.5, 1.0, 2.0, and 4.0 μM. Cells were treated for 24 h at 37˚C under 5% CO_2 atmosphere, consistent with standard protocols for cytotoxicity assessment.

Flow cytometric analysis of cell cycle and apoptosis. Cell cycle progression was analyzed using the BD Cycletest Plus DNA Reagent Kit (cat. no. 340242; Becton, Dickinson and Company), and apoptosis was assessed with the BD Annexin V-FITC Apoptosis Detection Kit I (cat. no. 556547; Becton, Dickinson and Company). Cells were seeded into 6-well plates at a density of $3x10^5$/well. After 24 h, the cells were treated with 0.1% DMSO (negative control), compound 1 (3.0, 6.0 and 9.0 μM) for 48 h at 37˚C. The cells were washed twice with cold PBS and then resuspended in 100 μl of binding buffer. Annexin V PE (5 μl) and 7-AAD (5 μl) were added, and the mixture was incubated in the dark at 37˚C for 15 min. Apoptosis and cell cycle distribution were analyzed using flow cytometry (NovoCyte 2040R; ACEA Biosciences, Inc.) (24).

RNA-Sequencing (RNA-seq) and data analysis. HeLa cells were pretreated with compound 1 at 6.0 μM for 24 h at 37˚C and then cells were washed with PBS and subsequently lysed directly in the culture dish using 1.5 ml of Trizol™ reagent (cat. no. 15596026CN; Invitrogen; Thermo Fisher Scientific, Inc.). The lysis process was allowed to proceed for 10 min at room temperature. Following lysis, the lysate was transferred to a 2.0 ml sterile centrifuge tube and stored at -80˚C for subsequent RNA extraction. Total RNA was extracted using Trizol™ reagent following the manufacturer's protocol. RNA concentration was measured using a NanoDrop 2000 spectrophotometer (Thermo Fisher Scientific, Inc.) and RNA integrity was assessed using an Agilent 2100 Bioanalyzer (Agilent Technologies, Inc.). RNA libraries were constructed and the sequencing was performed using the NovaSeq 6000 S4 Reagent Kit (300 cycles; cat. no. 20028315; Illumina, Inc.) and sequences using the Illumina HiSeq platform (New England Biolabs, Inc.). The library loading concentration was 0.5 nM, and quantification was conducted using qPCR. Paired-end sequencing with a read length of 150 bp (PE150) was carried out. The mRNA reads were mapped to the reference genome using HISAT2 software (version 2.2.1; https://ccb.jhu.edu/software/hisat/index.shtml). Gene expression was quantified as fragments per kilobase of exon model per million mapped reads, based on the number of uniquely mapped reads. Differential expression analysis was carried out using edgeR software (version 3.32.1; parameters: $P<0.05$; fold change ≥1.5). The results were visualized using a volcano plot, revealing differentially expressed metabolism-related genes and lncRNAs in cervical cancer and adjacent samples. Gene ontology (GO) enrichment and Kyoto Encyclopedia of Genes and Genomes (KEGG) pathway enrichment analyses were conducted using the clusterProfiler R package and the iDEP 1.1 web tool (https://bioinformatics.sdstate.edu/idep96/) (25). Heatmap analysis was performed using TBtools 2.200 (26), red represents upregulated gene expression.

Reverse transcription-quantitative PCR (RT-qPCR) for transcriptomics. HeLa cells were seeded in 12-well plates overnight and pretreated with compound 1 at different concentrations (3.0, 6.0 and 9.0 μM) at 37˚C for 24 h. Total RNA was extracted from the cells using TRIzol® reagent (Invitrogen; Thermo Fisher Scientific, Inc.) and cDNA was synthesized using the HiScript cDNA Synthesis Mix kit (Jiangsu CoWin Biotech Co., Ltd.). RT-qPCR was carried out using the UltraSYBR Mixture (With ROX) kit (Jiangsu CoWin Biotech Co., Ltd.). GAPDH was used as the internal reference gene. The primer sequences for TGIF2, ID1 and BMP2 were obtained from previous publications (Table SI). The PCR reaction mixture contained 2.0 μl cDNA template, 21.0 μl DNase-free ddH_2O, 1.0 μl forward and reverse primers, and 25.0 μl Ultra SYBR Mixture. The relative mRNA expression levels were measured using the Real-Time PCR Detection System (CFX Connect; Bio-Rad Laboratories, Inc.). qPCR was performed using the following thermocycling protocol: Initial pre-denaturation at 95˚C for 5 min; 35 cycles consisting of denaturation at 95˚C for 45 sec, annealing at 56˚C for 50 sec, and extension at 72˚C for 40 sec; followed by a final extension step at 72˚C for 5 min. The relative expression ratio was using the $2^{-\Delta\Delta Cq}$ method (27).

Molecular docking studies. Crystal structures of TGIF2 [Protein Data Bank (PDB) code, 2dmn], ID1 (PDB code, 6mgn) and BMP2 (PDB code, 1rew) were obtained from the Research Collaboratory for Structural Bioinformatics Protein Data Bank (https://www.rcsb.org/). The docking parameters were calculated using PyMOL 2.2.0 (https://github.com/schrodinger/pymol-open-source; center and size for the docking box were defined as follows, TGIF2: Center_x, -3.094; center_y, -3.281; center_z, 3.948 with size_x, 65.45; size_y, 65.45; size_z, 65.45; ID1: Center_x, 18.573; center_y, 14.631; center_z, 12.395 with size_x, 46.55; size_y, 46.55; size_z, 46.55; BMP2: Center_x, -28.157; center_y, 67.095; center_z, 21.448 with size_x, 65.45; size_y, 65.45; size_z, 65.45). Molecular docking studies were carried out to explore the binding modes of compound 1 with TGIF2, ID1 and BMP2 using AutoDock Vina 1.2.3 (https://github.com/ccsb-scripps/AutoDock-Vina/releases/tag/v1.2.3). The best-scoring docking poses were selected based on the Vina docking scores and further analyzed visually using PyMOL 2.2.0 and Discovery Studio 2021 software (Version 21.1.0.20298; https://www.3ds.com/products-services/biovia/products/molecular-modeling-simulation/biovia-discovery-studio/).

Molecular dynamics simulation. MD simulations were carried out using the Amber24 software suite (version 2024; https://ambermd.org/) (28), applying the ff19SB force field (29,30) and the OPC water model (31). The complex was placed in a cubic water box, with electrostatic and van der Waals interactions having cut off distances set to 1.0 nm. A time step of 2 fs was used for the integration and long-range electrostatic interactions were handled using the Particle Mesh Ewald

method (32). The system was maintained at a temperature of 300 K and a pressure of 1 bar. Initial energy minimization was carried out (33), followed by 200 ps of constant number of particles, volume, and energy equilibration and 100 ps of constant number of particles, pressure, and temperature equilibration dynamics. Temperature control was achieved using the V-rescale method (34), while pressure control was applied using the Parrinello-Rahman approach (35). Following the equilibration, 200 ns of production dynamics were carried out. Key metrics such as root mean square deviation (RMSD), root mean square fluctuation (RMSF), radius of gyration (Rg) and hydrogen bond counts were calculated using Amber's built-in Cpptraj tool.

Statistical analysis. Data analysis was carried out using SPSS Statistics 21.0 (IBM Corp.) and GraphPad Prism 7.0 (Dotmatics). Results are presented as the mean ± SD of three independent experiments. Statistical analysis was conducted using the unpaired Student's t-test or the one-way or two-way ANOVA, followed by Šídák's multiple comparisons test. $P<0.05$ was considered to indicate a statistically significant difference.

Results

Compounds from Alternaria semiverrucosa and cytotoxic activity assay. Structures of the ten known compounds were identified (Fig. S1) as i) DAP (Figs. 1A, S2 and B) (36), ii) Fonsecinone A (Fig. S3A and iii) (37), Aurasperone A (Fig. S4A-B) (38), iv) 3β,5α,9α-trihydroxy-(22E,24R)-ergosta-7,22-diene-6-one (Fig. S5A and B) (30), v) Gargalol B (Fig. S6A and B) (39), vi) (22E,24R)-ergosta-7,22-dien-3β,5α,6β,9α-tetraol (Fig. S7A and B) (40), vii) 11-[(6-Deoxy-α-L-mannopyranosyl)oxy]-3-hydroxyhexadecanoic acid (Fig. S8A and B), viii) Penisochroman A (Fig. S9A and B) (41), viiii) β-adenosine (Fig. S10A and B) (42) and x) uridine (Fig. S11A and B) (43), by comparing their 1H, 13C NMR (Data S1) and mass spectrometry data with those in the literature.

The aforementioned compounds were tested for cytotoxicity *in vitro* against human tumor cell lines (PC3, LNCaP, HeLa, SiHa, K562, and HEL). As shown in Table SII, compound 1 exhibited an inhibition rate of 49.48% against HeLa cells, and demonstrated the most potent inhibitory effect. HeLa cells were exposed to varying concentrations of 2.5, 5.0, 10.0, 20.0 and 40.0 μmol/l for 24, 48 and 72 h. As illustrated in Fig. 1B, within the same time frame, the inhibitory effect on cell proliferation became progressively more pronounced with increasing treatment concentration. However, when considering the duration of exposure, the inhibitory effect diminished over time. Statistical analysis indicated IC_{50} values of 6.43±3.03 μmol/l at 24 h, 8.80±1.19 μmol/l at 48 h and 19.27±0.55 μmol/l at 72 h (Fig. 1B). This was significantly higher when compared with the positive control (IC_{50}=1.20±0.20 μM; Fig. 1C) at 24 h ($P=0.0310$).

Compound 1 was also tested in normal HGF-1 cells as a reference, and exhibited a markedly reduced inhibitory effect when compared with the HeLa cells ($P=0.0055$), with an IC_{50} value of 54.10±0.10 μmol/l (Fig. 1D), suggesting limited cytotoxic activity. The safety profile of a drug is typically assessed using the selectivity index (SI), which is defined as: SI=IC_{50} (normal cells)/IC_{50} (tumor cells), with a SI value of 8.41. An increased SI value indicates a broader therapeutic window and reduced cytotoxicity towards normal cells. Morphological changes in the cells became apparent after 24 h of treatment compared with the control group (Fig. 1E). As drug concentration increased, intercellular spaces widen, cellular morphology becomes more rounded, and the presence of cell debris becomes increasingly evident.

DAP induced apoptosis and cell cycle G1/S arrest in HeLa cancer cells. Compound 1 was subsequently evaluated for its effects on the cell cycle and apoptosis. As shown in Fig. 2A and B, these findings suggest that compound 1 induces apoptosis in HeLa cells. Notably, the proportion of early apoptotic cells was reduced compared with that of late apoptotic cells after a 24 h treatment with compound 1 ($P=0.0065$), indicating that the majority of the cytotoxic effects of compound 1 on HeLa cells are due to the induction of late-stage apoptotic cell death. The impact of compound 1 on cell cycle distribution was evaluated using flow cytometry. As illustrated in Fig. 2C, compared with the control group, alterations in the G1 and S phases were observed with increasing concentrations of compound 1. Statistical analysis (Fig. 2D) revealed that when the concentration of compound 1 reached 6.0 μmol/l, the proportion of HeLa cells in the G1 phase was significantly reduced compared with the control group ($P=0.0126$), with a significant decrease observed at 9.0 μmol/l ($P=0.0090$). By contrast, cell accumulation was evident in the S phase. A significant increase in the S phase population was detected at a concentration of 3.0 μmol/l ($P=0.0280$), which further increased markedly at 6.0 μmol/l ($P=0.0043$). No notable changes were observed in the G2/M phase. These findings suggest that the growth inhibitory effect of compound 1 on HeLa cells is associated with cell cycle arrest in the S phase.

Transcriptome analysis. To further investigate the molecular mechanisms underlying the effects of DAP, transcriptome sequencing (RNA-seq) was carried out in HeLa cells. This analysis identified 140 differentially expressed genes (DEGs), including 99 upregulated and 41 downregulated genes (Fig. 3A and B). GO and KEGG enrichment analyses revealed significant enrichment in pathways associated with tumor cell proliferation, particularly the Hippo signaling and TGFβ signaling pathways (Fig. 3C) have been implicated in the regulation of cell apoptosis. Among the pathways enriched with a $P<0.05$ (Fig. 3C), two apoptosis-related signaling pathways, specifically the TGF-β signaling pathway and the Hippo signaling pathway, were identified. Within the TGF-β signaling pathway, the differentially expressed genes were TGIF2, BMP2, and ID1; in contrast, the Hippo signaling pathway exhibited differential expression of TGIF2 and BMP2. Collectively, three distinct differentially expressed genes (TGIF2, BMP2, and ID1) were observed across both signaling pathways. GO analysis was conducted on DEGs to elucidate the molecular mechanisms underlying their regulation. In the cellular component category (Fig. 3D), significant enrichment was observed for postsynaptic density ($P=0.00052$), Golgi apparatus ($P=0.00099$), dendritic tree ($P=0.00162$), catalytic complex ($P=0.00294$) and dendritic spine ($P=0.00392$). In the biological process category (Fig. 3E), notable terms included ‘negative regulation of epithelial

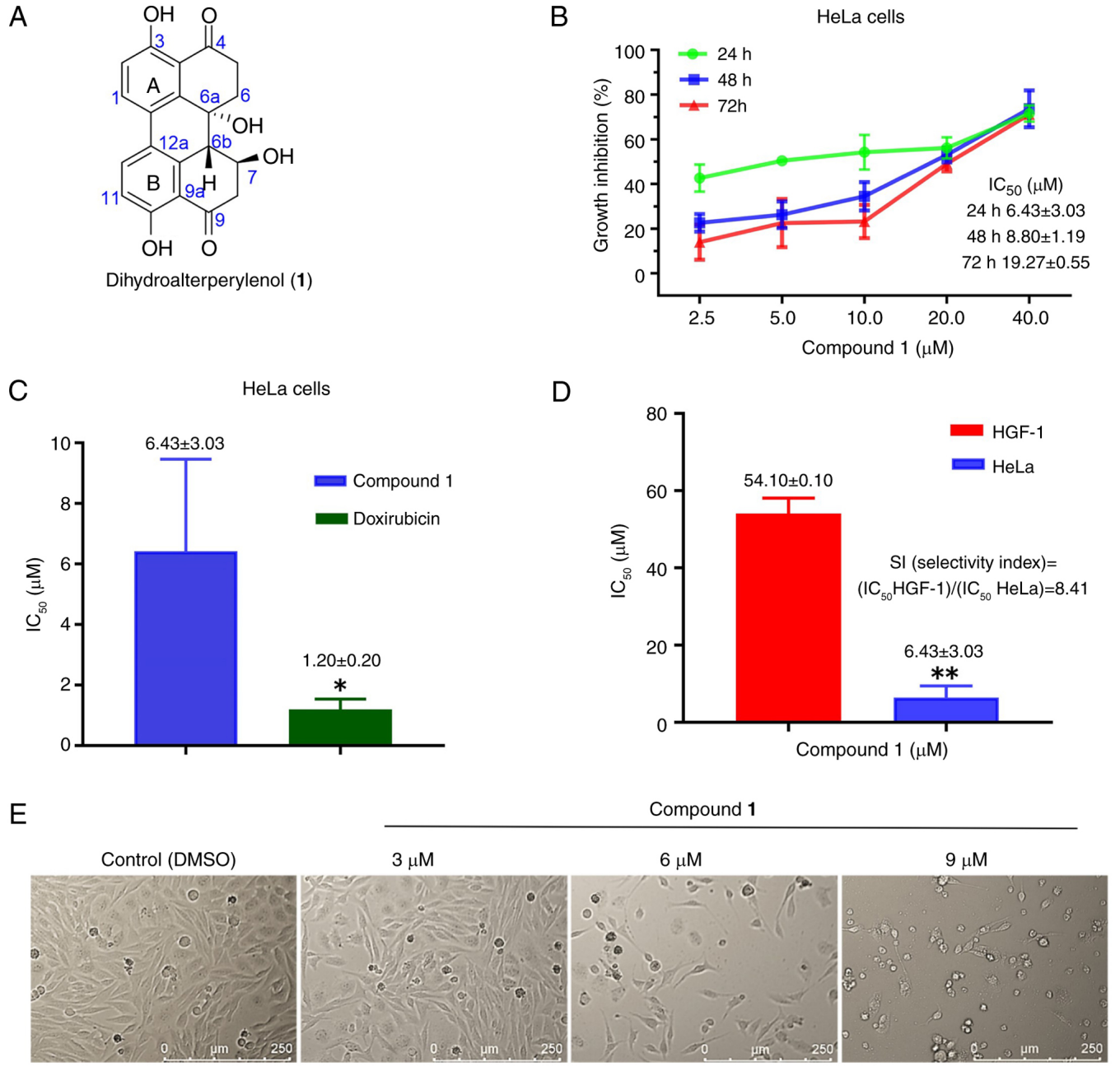

Figure 1. Effect of compound 1 on HeLa cells. (A) Chemical structure of compound 1; (B) IC_{50} values of compound 1 on HeLa cell proliferation at 24, 48 and 72 h; (C) Comparison of the IC_{50} values of compound 1 and doxorubicin on HeLa cell proliferation; (D) Comparison of the compound 1 IC_{50} value between HGF-1 and HeLa cells; (E) Morphological changes of HeLa cells. HGF-1, human gingival fibroblasts. *P<0.05 vs. the doxorubicin group (n=3) , **P<0.01 vs. the HGF-1 group (n=3).

cell proliferation' (P=7.20x^{-06}), 'single-organism cellular process' (P=1.90x^{-05}), 'negative regulation of cell proliferation' (P=2.50x^{-05}), 'positive regulation of transcription from RNA polymerase II promoter' (P=3.30x^{-05}) and 'single-organism process' (P=0.00012). In the molecular function category (Fig. 3F), enriched terms were 'protein kinase binding' (P=0.00032), 'identical protein binding' (P=0.00125), 'ATPase activity coupled to transmembrane movement of substances' (P=0.00131), 'protein binding, bridging' (P=0.0042) and 'cysteine-type peptidase activity' (P=0.0043). The GO analysis indicated that the inhibitory effect of compound 1 on HeLa cell proliferation was primarily associated with the regulation of cellular proliferation processes.

mRNA expression of DAP in HeLa cells. To investigate the expression patterns of key genes in the TGFβ signaling pathway and Hippo signaling pathway, TGIF2, ID1 and BMP2 were selected. Heatmaps were generated using TBtool (https://gitee.com/an-jiaxin/TBtools), revealing that all three genes exhibited significant upregulation compared with the control group (Fig. 4A). Additionally, RT-qPCR analysis was conducted to evaluate the expression levels of these genes under treatment with different concentrations of compound 1. Compared with the control group, the expression levels of all three genes were increased. Specifically, the expression of TGIF2 and ID1 showed a significant increase at 9.0 μmol/l compound 1 (P=0.0006 and P=0.0215), while BMP2

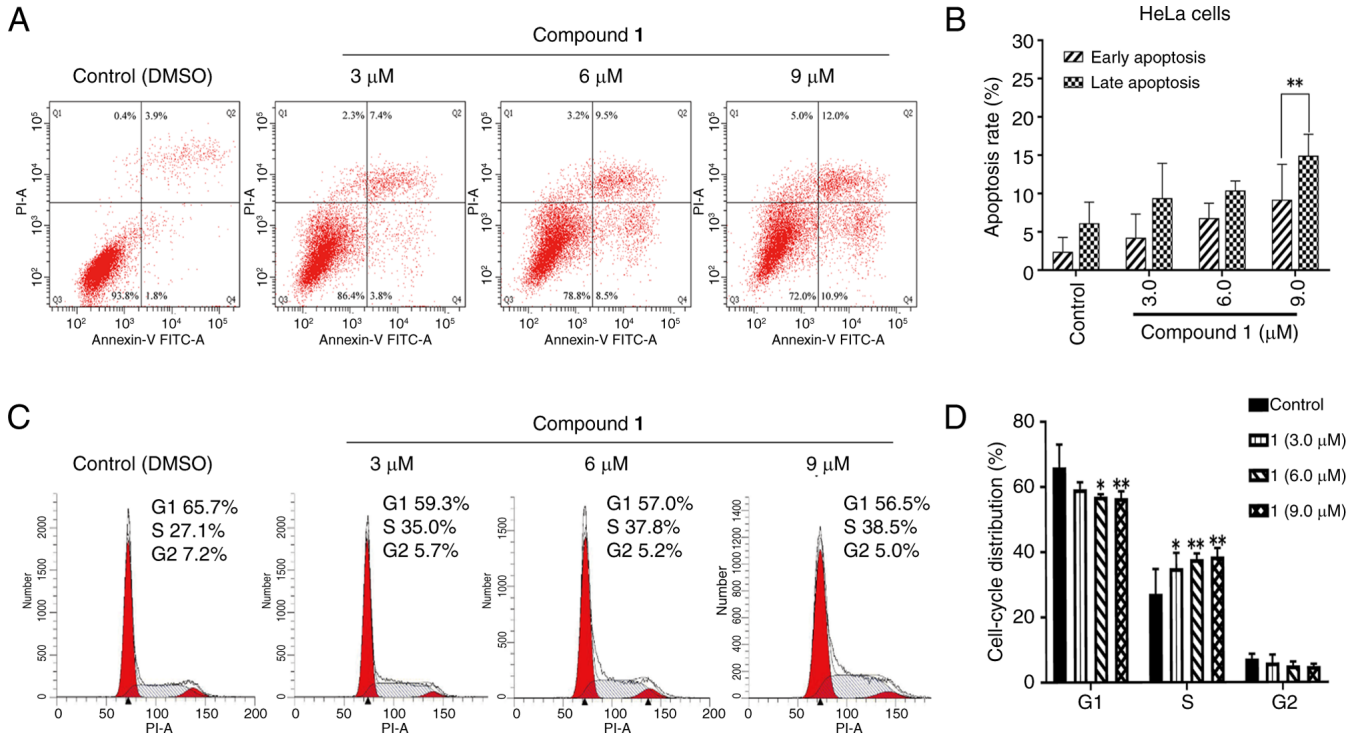

Figure 2. Apoptosis and cell cycle arrest efects of HeLa cells induced by compound 1. (A) Apoptosis was assessed by annexin V-FITC/PI staining after treatment with compound 1 for 24 h, followed by flow cytometric analysis; (B) Statistical analysis of early and late apoptosis rates in HeLa cells; (C) Cell cycle distribution was evaluated by PI staining after treatment with compound 1 for 24 h and analyzed by flow cytometry; (D) Percentage of HeLa cells in each phase of the cell cycle. *P<0.05, **P<0.01 vs. the control group (n=3).

expression significantly increased at 3.0 μmol/l Compound 1 (P=0.0035) (Fig. 4B). These results indicate that the gene expression trends observed in transcriptome sequencing are consistent with those obtained from RT-qPCR analysis, verifying that the expression levels of TGIF2, ID1 and BMP2 are upregulated following compound 1 treatment.

Docking studies of DAP with TGIF2, ID1 and BMP2. Molecular docking studies were conducted to explore the potential binding sites of compound 1 with TGIF2, ID1 and BMP2. The docking results revealed that the binding energies between compound 1 and TGIF2, ID1 and BMP2 were all <-5.0 kcal/mol (Table SIII). Specifically, a hydrogen bond was formed between the 7-OH group of compound 1 and Trp57 of TGIF2 (Fig. 5A). Additionally, π-Cation and π-Sigma interactions were observed between the two benzene rings of compound 1 and Arg64 and Ile65. For ID1, a hydrogen bond was formed between the 7-OH group of compound 1 and Gln583, while the A-ring of compound 1 interacted with Arg567 of ID1, with distances of 1.92 Å and 5.11 Å, respectively (Fig. 5B). As shown in Fig. 5C, a hydrogen bond interaction was observed between 7-OH of compound 1 and the carbonyl group (C-4) of BMP2, with distances of 3.43 Å and 2.53 Å, respectively. Furthermore, the benzene B-ring of compound 1 interacted with Ile87 of BMP2 via a π-σ bond.

RMSD. RMSD is a key indicator of protein conformational variability, providing insights into the stability of ligand-target protein interactions. Higher RMSD values indicate greater structural alterations within the complex, while lower values suggest more stable binding configurations (44). As shown in Fig. 6A, the BMP2-1rew complex exhibited notable fluctuations in RMSD during the initial phase of the simulation (0-10 ns) before stabilizing between 10 and 200 ns. Similarly, the ID1-6mgn complex displayed considerable RMSD variations from 0 to 80 ns, followed by stabilization from 80 to 200 ns. The TGIF2-2dmn complex also experienced considerable RMSD fluctuations during the first 155 ns, ultimately stabilizing from 155 to 200 ns. These results indicate that all three complexes, BMP2-1rew, ID1-6mgn and TGIF2-2dmn underwent substantial conformational changes early in the simulation before achieving stability at different time intervals.

RMSF. RMSF measures the flexibility of individual amino acid residues during MD simulations. Higher RMSF values indicate increased flexibility at specific residues (45). As depicted in Fig. 6B, the BMP2-1rew complex exhibited fluctuations at residues 58-63, 83-85 and 104. The ID1-6mgn complex revealed marked mobility in residues 1-4 and 48-53, while the TGIF2-2dmn complex demonstrated considerable movement in residues 1-4 and 79-84. Despite these localized fluctuations, the overall structural stability of all three complexes, BMP2-1rew, ID1-6mgn and TGIF2-2dmn, remained relatively intact.

Radius of gyration (Rg). Rg radius is an important metric for evaluating the compactness of molecular structures. Higher Rg values suggest a more extended conformation, while lower values indicate a more condensed structure (46). As shown in Fig. 6C, after equilibration, the BMP2-1rew complex exhibited minimal fluctuations and stabilized at ~1.86 nm. The ID1-6mgn

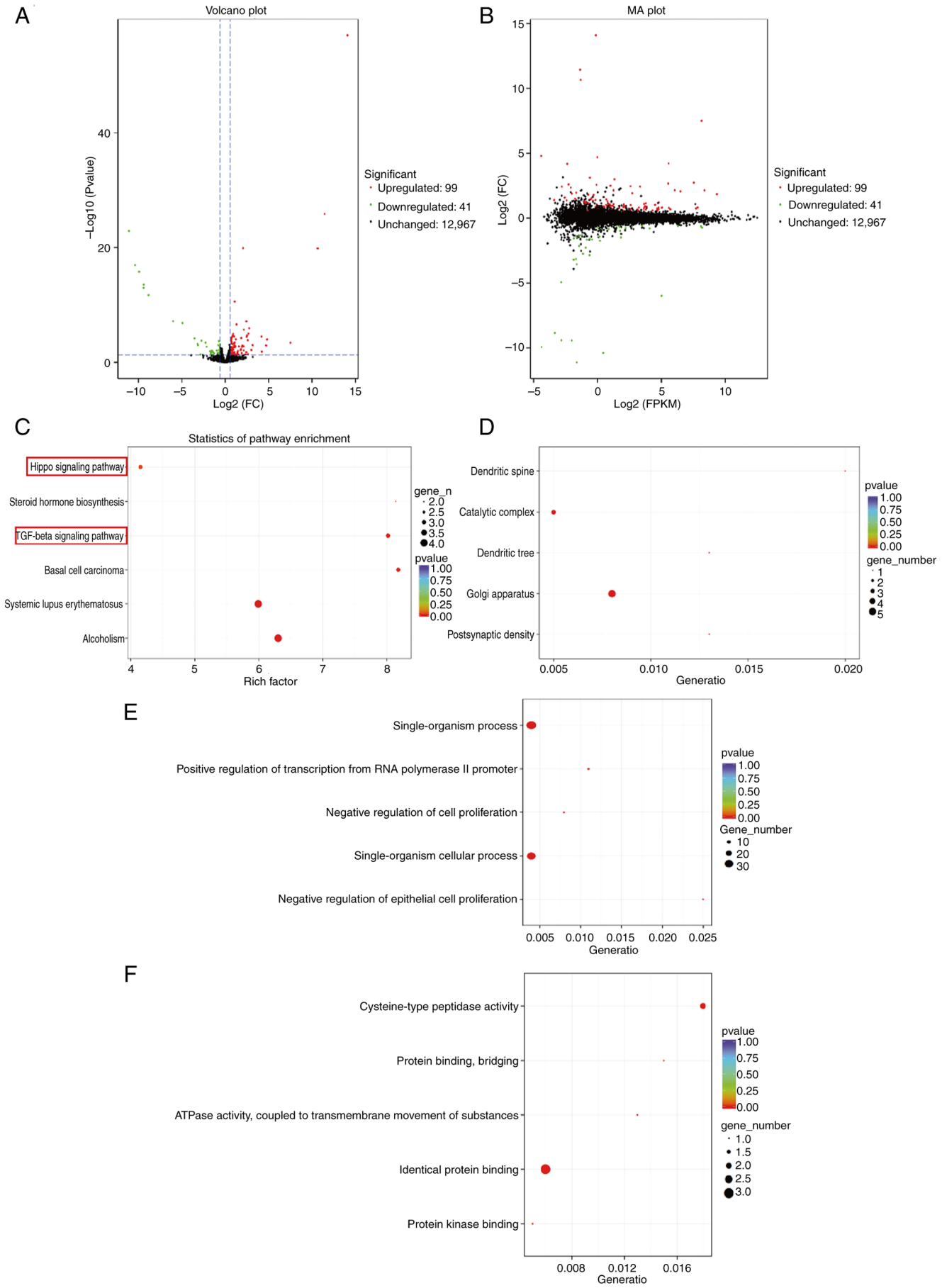

Figure 3. mRNA transcriptomic analysis in HeLa cells treated with Dihydroalterperylenol. (A) Volcano map; (B) MA plot of differentially expressed genes; (C) Kyoto Encyclopedia of Genes and Genomes pathway enrichment; (D) cellular component; (E) biological process and (F) molecular function. MA, Minus-versus-Add.

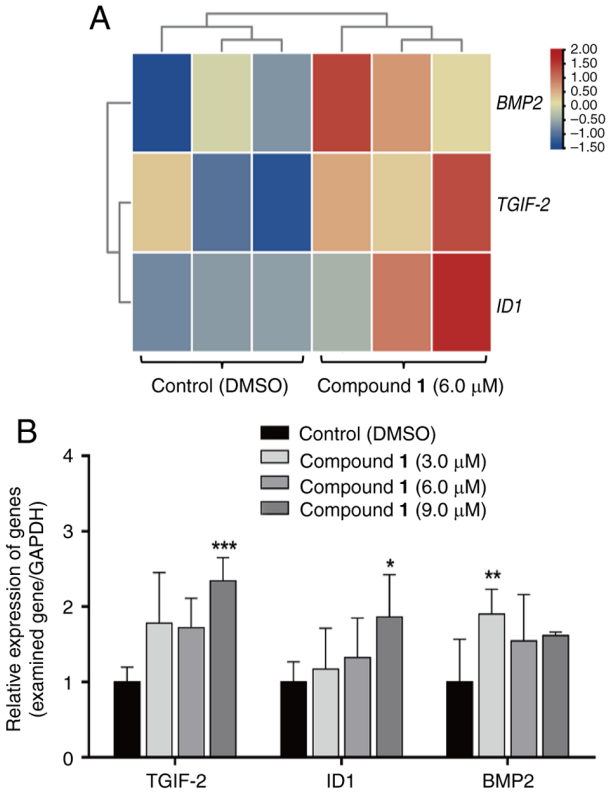

Figure 4. Thermogram of differential gene expression in Hela cells treated with compound 1 and reverse transcription-quantitative PCR analysis at different concentrations (3.0, 6.0 and 9.0 μM). (A) Differential expression heatmap of BMP2, TGIF-2 and ID1 genes; (B) Relative mRNA expression levels of BMP2, TGIF-2 and ID1 genes. *P<0.05; **P<0.01; ***P<0.001 vs. control (DMSO; n=3).

complex revealed limited variation, stabilizing at ~1.08 nm. Similarly, the TGIF2-2dmn complex demonstrated minor fluctuations, stabilizing at ~1.52 nm. These results suggest that the BMP2-1rew complex adopts a relatively extended conformation, indicative of weaker intermolecular interactions. By contrast, the ID1-6mgn complex adopts a more compact structure, implying stronger intermolecular interactions. The TGIF2-2dmn complex falls in between, revealing moderate intermolecular interactions.

Solvent-accessible surface area (SASA). SASA quantifies the exposure of protein molecules to their surrounding water environment, reflecting changes in hydrophobic and hydrophilic properties (47). As shown in Fig. 6D, SASA values for the entire system remained relatively stable throughout the simulation. Among the three complexes, the ID1-6mgn complex exhibited the most compact structure, followed by TGIF2-2dmn, with BMP2-1rew displaying the least compact conformation. These findings suggest that the ID1-6mgn complex likely has the strongest intermolecular interactions, while the BMP2-1rew complex likely exhibits the weakest.

Hydrogen bonds. Hydrogen bonds are among the strongest non-covalent interactions and serve as important indicators of binding strength during molecular simulations (48). The frequency and number of hydrogen bonds observed in the simulations reflect the dynamic nature of protein-ligand interactions. A higher number of hydrogen bonds typically correlates with greater binding stability (48). As shown in Fig. 6E, the BMP2-1rew complex formed between 1 and 3 hydrogen bonds, whereas both the ID1-6mgn and TGIF2-2dmn complexes formed between 1 and 4 hydrogen bonds. These findings suggest that the interactions within the ID1-6mgn and TGIF2-2dmn complexes are likely more robust compared with those observed in the BMP2-1rew complex.

Combination free energy. Molecular mechanics generalized born surface area is a method (49) that is widely employed post-simulation to estimate the binding free energy of molecular complexes, providing insights into their stability. A lower binding free energy value suggests a stronger binding affinity (49). As shown in Fig. 7A, the key residues contributing to the binding free energy of the BMP2-1rew complex include ARG-5, HIE-28, PHE-30, TYR-27, VAL-96, ILE-76, ALA-29, TYR-9, PRO-7 and PRO-24 from the protein. The binding free energy for this complex is calculated at -19.74 kcal/mol, with contributions from van der Waals interactions (-18.04 kcal/mol), electrostatic potential energy (-30.87 kcal/mol) and non-polar solvation effects (-1.63 kcal/mol; Fig. 7B).

For the ID1-6mgn complex (Fig. 7C), the binding free energy primarily involves residues ALA-25, GLN-17, ARG-10, GLN-26, PHE-9, ASN-6, ILE-31, ARG-14, LYS-24 and GLY-13. The calculated binding free energy is -22.04 kcal/mol, with van der Waals forces contributing -23.73 kcal/mol, electrostatic potential energy contributing -28.32 kcal/mol and non-polar solvation energy contributing -2.31 kcal/mol (Fig. 7D).

For the TGIF2-2dmn complex (Fig. 7E), the binding free energy involves residues ARG-64, TRP-57, LEU-14, ALA-61, ASN-60, ILE-65, ASN-13, VAL-19, LEU-22 and ASN-56, with the overall binding free energy calculated as -21.43 kcal/mol (Fig. 7F). The contributions include van der Waals forces (-29.43 kcal/mol), electrostatic potential energy (-21.26 kcal/mol) and non-polar solvation energy (-2.26 kcal/mol).

These results indicate that DAP exhibits strong binding affinities with TGIF2, ID1 and BMP2, with van der Waals and electrostatic interactions carrying out the most significant roles, while non-polar solvation energy contributes to a lesser extent. Polar solvation energy appears to have a less favorable effect on these interactions.

Free energy landscape (FEL). FEL provides a detailed characterization of the free energy changes experienced by a molecular system during simulations. By analyzing the FEL, the characteristic conformations of a complex can be identified and examined, which serves as an indicator of conformational stability during the simulation (50,51). As illustrated in Fig. 8, the BMP2-1rew complex predominantly adopts a stable conformation within an RMSD range of 0.10-0.30 Å and an Rg range of 1.77-1.90 nm (Fig. 8A). For the ID1-6mgn complex, the most stable conformation is observed within an RMSD range of 0.0-0.7 Å and an Rg range of 1.0-1.4 nm (Fig. 8B). The TGIF2-2dmn complex demonstrates two distinct regions of dominant stability: One with an RMSD of 0.0-1.2 Å and Rg of 1.3-1.8 nm, and another

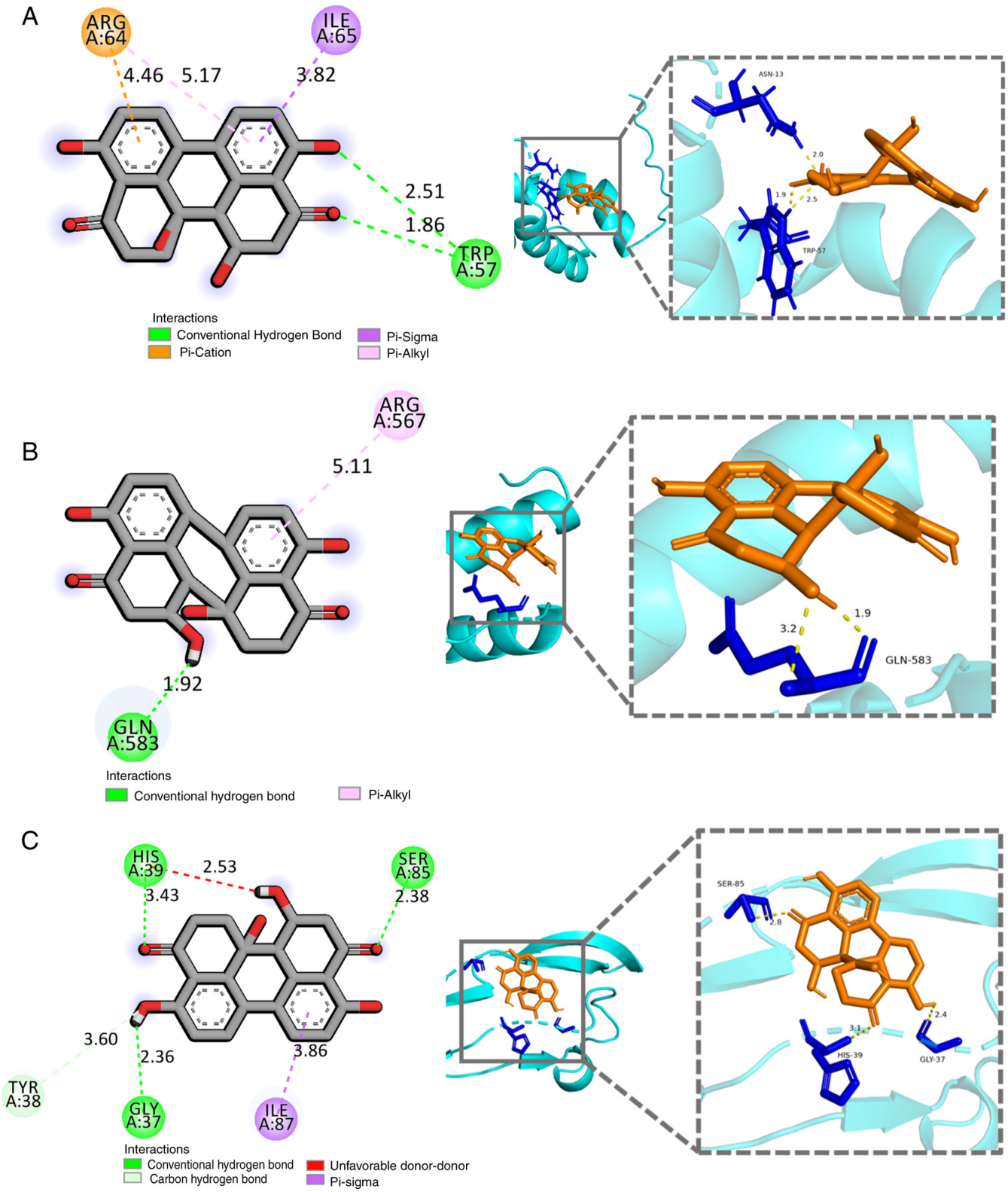

Figure 5. Docking interaction between compound 1 and (A) TGIF2, (B) ID1 and (C) BMP2.

with an RMSD of 0.8-1.0 Å and Rg of 1.45-1.55 nm (Fig. 8C). These findings indicate that the BMP2-1rew, ID1-6mgn and TGIF2-2dmn complexes each exhibit stable conformations within specific RMSD and Rg ranges, which can be utilized as a basis for understanding the characteristic conformations and stability of these complexes.

Discussion

Treatment of cervical cancer currently relies on a combination of surgery, radiotherapy, chemotherapy and immunotherapy (52). Early-stage cervical cancer can often be managed with either radical surgery or radiation therapy (53).

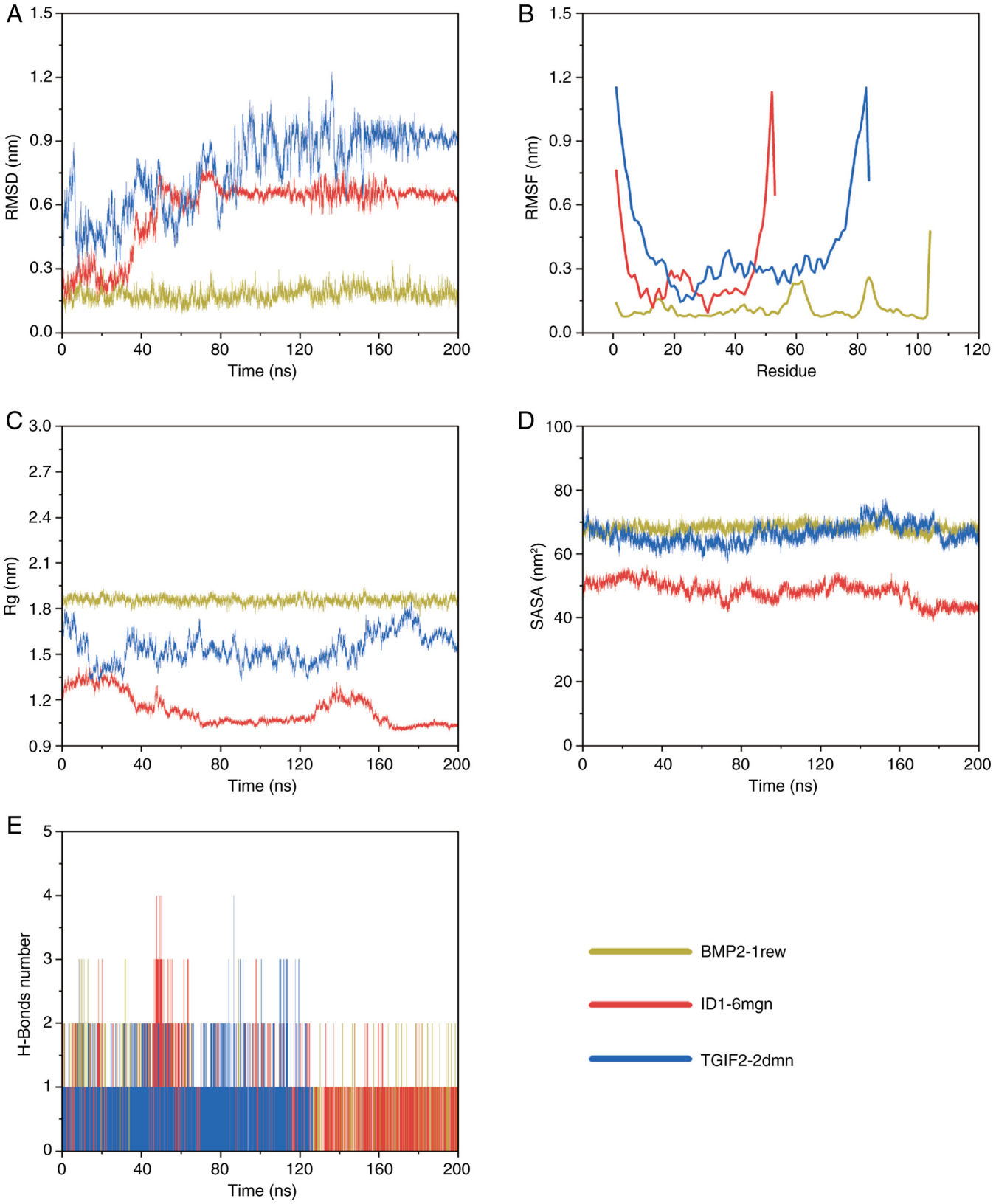

Figure 6. Results of molecular dynamics simulation. (A) RMSD variation curve; (B) fluctuation of amino acid residues; (C) Rg curve; (D) SASA fluctuation curve; (E) Number of H bonds. RMSD, root mean square deviation; RMSF, root mean square fluctuation; Rg, gyration; SASA, solvent-accessible surface area; H-bonds, hydrogen bonds.

However, both methods suffer from a lack of specificity for cancer cells, leading to notable side effects despite their clinical efficacy. Traditional chemotherapy agents for cervical cancer, such as nedaplatin, paclitaxel and bleomycin, are associated with harmful side effects (54,55). Consequently, there is a need for more effective and safer anticancer drugs.

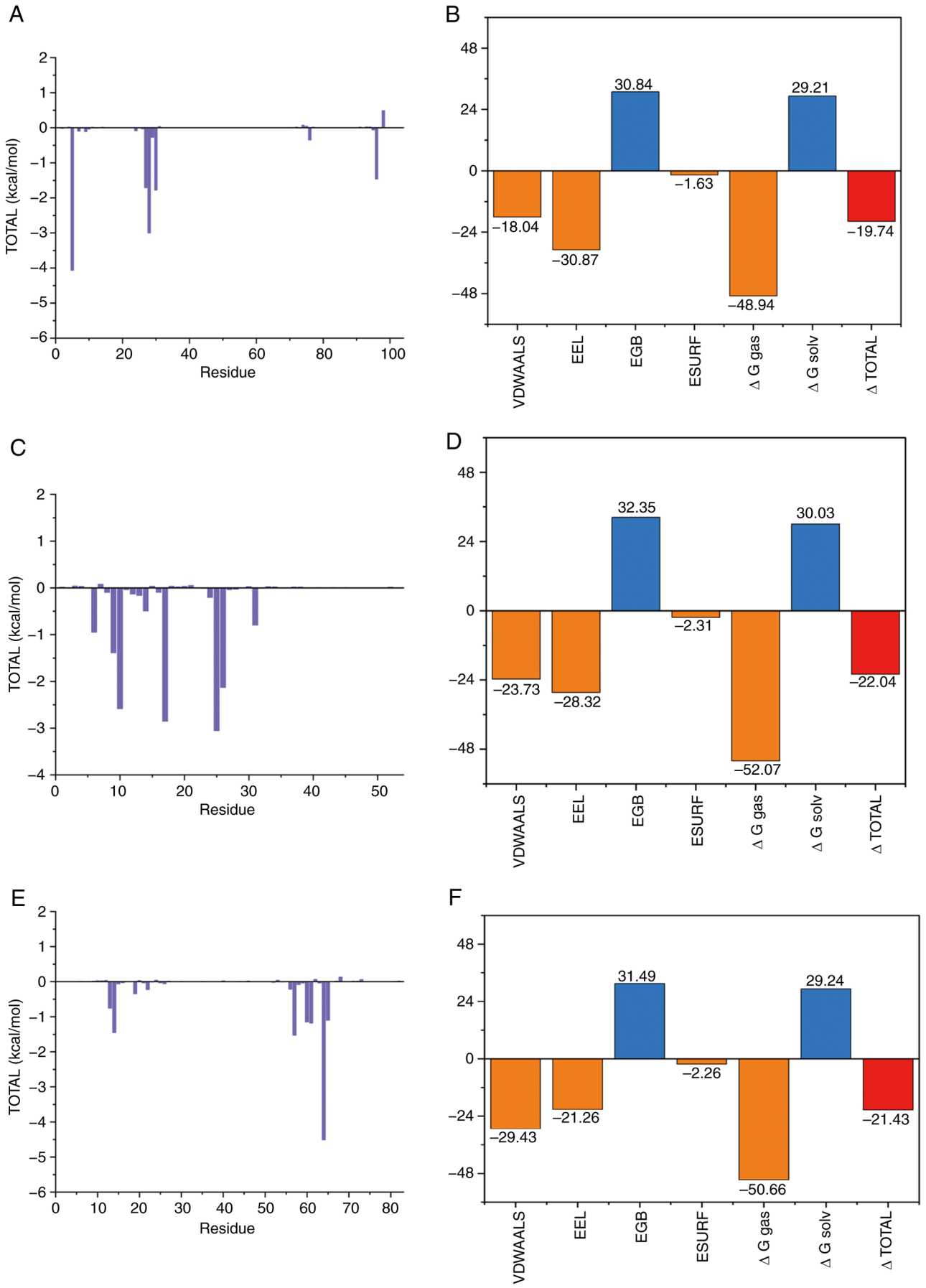

Figure 7. Molecular dynamics simulation energy analysis. (A) Energy contribution of each amino acid residue in the protein-ligand complex (BMP2-1rew); (B) Total binding energy of the protein-ligand complex (BMP2-1rew); (C) Energy contribution of each amino acid residue in the protein-ligand complex (ID1-6mgn); (D) Total binding energy of the protein-ligand complex (ID1-6mgn); (E) Energy contribution of each amino acid residue in the protein-ligand complex (TGIF2-2dmn); (F) Total binding energy of the protein-ligand complex (TGIF2-2dmn).

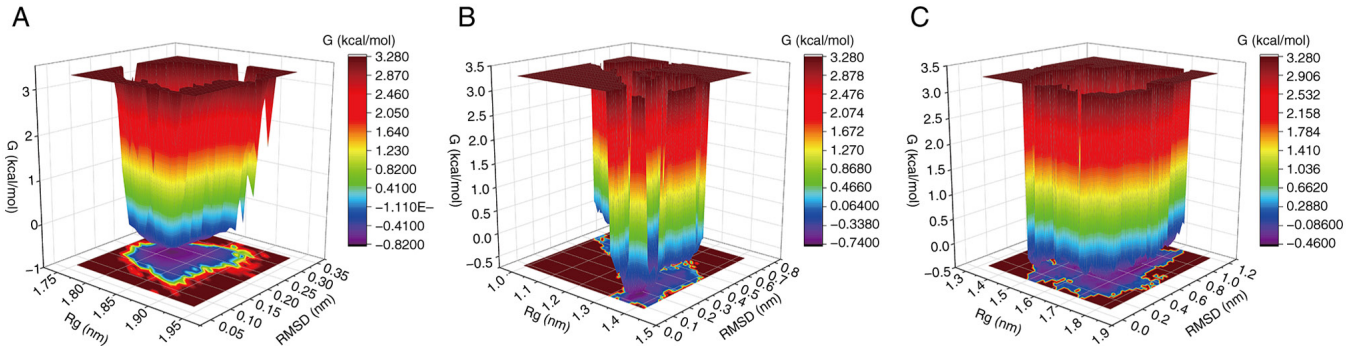

Figure 8. Free energy landscape of molecular dynamics simulation. (A) BMP2-1rew; (B) ID1-6mgn and (C) TGIF2-2dmn. RMSD, root mean square deviation

Natural products, known for their low toxicity and ability to target multiple biological pathways, have gained attention as promising alternatives to chemical drugs due to their superior biocompatibility (56). As a result, natural products have become a key source of novel antitumor agents (57).

DAP also known as Altertoxin I, is a quinone-type mycotoxin first isolated from *Alternaria* species. A previous study reveal that DAP has an ID_{50} value of 20 μg/ml against HeLa cells (58). DAP has been evaluated for cytotoxicity in A549, HeLa, U2OS and HepG2 cell lines, and the results revealed that DAP exhibited minimal cytotoxicity at 20 μM in these cell lines (43). DAP has demonstrated selective cytotoxicity against human colon cancer cells (HCT-8) with an IC_{50} of 1.78 μM (59), highlighting its potential in cancer therapy. Chemotherapy, a mainstay treatment, is frequently hampered by drug resistance and dose-limiting toxicities (60). Cisplatin remains the preferred drug for the chemotherapeutic treatment of cervical cancer, however, several factors, including its low selectivity, high toxicity, adverse side effects, tumor multidrug resistance and propensity for recurrence, ultimately contribute to treatment failure (61). Chemotherapy failure is primarily caused by drug resistance mechanisms, such as P-glycoprotein-mediated efflux of chemotherapeutic agents from tumor cells. Furthermore, chemotherapy is constrained by dose-limiting toxicities that adversely affect healthy tissues and compromise the quality of life of patients (62). Additionally, targeted therapies encounter obstacles due to tumor heterogeneity and the development of resistance through compensatory signaling pathways (63). Natural products such as DAP offer a promising strategy to address these issues. Its structural complexity enables multi-target mechanisms, potentially overcoming resistance while minimizing off-target effects. In the present study, DAP exhibited potent activity against HeLa cells (IC_{50}±6.43 μM) and transcriptome analysis revealed that DAP induces apoptosis via the Hippo and TGFβ pathways. This dual effect may circumvent common drug resistance mechanisms. Notably, DAP exhibited minimal inhibitory activity against HGF-1 after 24 h of exposure, with an SI value of 8.41. The safety profile of the drug was evaluated using the SI value, where a higher SI value indicates a broader therapeutic window and reduced cytotoxicity towards normal cells. A previous study has demonstrated that an SI value >1 is indicative of selective antitumor activity (64).

The findings of the present study demonstrated that the IC_{50} of DAP exhibits a time-dependent increase, indicating that prolonged exposure to drug treatment may enhance the fitness of a cell population. According to existing research findings (65), the fitness of a cell population can be improved through gradual exposure to stress, as cells epigenetically adapt and fine-tune their stress regulatory networks, thereby establishing stable adaptive states. Initially, drug-sensitive cells accumulate transcriptional and epigenetic changes in response to stress, resulting in more robust responses upon subsequent stimulation. We hypothesize that a comparable process occurs when DAP is applied to HeLa cells spanning an extended period, leading to an increase in IC_{50} from 6.43 μM at 24 h to 19.27 μM at 72 h.

DAP was applied to HeLa cells at concentrations of 3.0, 6.0 and 9.0 μmol/l for 24 h, inducing apoptosis and cell cycle arrest in a concentration-dependent manner. At the highest concentration of 9.0 μmol/l, the apoptosis rate reached 24.13%, with cell cycle arrest occurring predominantly in the S phase. These findings suggest that the inhibitory effects of DAP on HeLa cells are associated with apoptosis induction and cell cycle arrest. To further elucidate the molecular mechanisms underlying DAP-induced apoptosis, transcriptome sequencing was conducted on HeLa cells treated with 6.0 μmol/l DAP for 24 h, identifying 140 DEGs. Bioinformatics analysis using KEGG and GO revealed that significantly enriched pathways were associated with apoptosis, while GO annotations highlighted terms associated with the regulation of cell proliferation. Specifically, the TGFβ signaling pathway and Hippo signaling pathway, both implicated in apoptosis and enriched in KEGG, were analyzed in detail. Three genes (TGIF2, ID1 and BMP2) were identified as key mediates in these pathways. Subsequent RT-qPCR analysis confirmed that the expression trends of these three genes were consistent with the results from transcriptome sequencing. This consistency indicates that the inhibitory effects of DAP on HeLa cells are likely mediated through the upregulation of TGIF2, ID1 and BMP2.

TGIF2, an important member of the TGIF family, encodes a DNA-binding transcription factor that carries out a key role in tumor regulation through multiple mechanisms. The study has demonstrated that long non-coding RNA SNHG7 upregulates TGIF2 expression by modulating miR-449a, thereby promoting proliferation, migration, invasion and epithelial-mesenchymal transition in non-small cell lung cancer (66). Additionally, non-coding RNA MALAT1 upregulates TGIF2 expression by negatively regulating miR-129, leading to enhanced proliferation, migration and invasion in human osteosarcoma MG63

cells (67). In osteosarcoma, TGIF2 serves as a target gene of miR-34; its upregulation inhibits osteosarcoma tumor growth in nude mice and promotes apoptosis (68), these findings are consistent with the upregulation of TGIF2 expression observed in cervical cancer HeLa cells in the present study.

ID1 is a member of the helix-loop-helix (HLH) family of transcription factors. ID1 exerts its oncogenic effects by inhibiting the activity of basic HLH transcription factors, thereby participating in tumor initiation, progression, cell cycle regulation and metastasis. It is closely associated with angiogenesis, tumor differentiation and drug resistance in various types of cancer (69,70). As a negative regulator of cell differentiation, ID1 promotes tumorigenesis by activating the MAPK signaling pathway and inactivating the p16(INK4a)/pRB tumor suppressor pathway, thus facilitating the growth and proliferation of prostate cancer cells (71,72). A study has confirmed that ID1 is highly expressed in ovarian cancer tissues and its expression associates with the degree of tumor differentiation, carrying out a key role in ovarian cancer development (73). Compared with control cells, SKOV3 cells depleted of ID1 exhibited a notable reduction in proliferation and invasion capabilities, while apoptosis was markedly increased (74). The increase in ROS levels following ID1 overexpression aligns with prior studies revealing ROS inhibits dendritic cell differentiation and myeloid-derived suppressor cell expansion in tumor-bearing mice (75), These findings are consistent with the results of the present study. We hypothesize that DAP upregulates ID1 expression, increasing ROS levels and inhibiting cervical cancer cells.

BMP2 is a highly expressed secreted protein in various types of cancer (76). As a member of the TGFβ superfamily, BMP2 participates in multiple biological processes, including normal cell growth and development, apoptosis, migration, invasion, bone formation and cancer progression (77). Research (78) indicates that BMP2 carries out a key role in the proliferation, migration and differentiation of neural crest cells. Compared with normal tissues, BMP2 is considerably upregulated in various cancer tissues, suggesting its potential as a key biomarker for targeted cancer therapy. Literature studies have revealed that BMP2 exhibits both pro-cancer and anti-cancer functions in cancer tissues. For instance, Du *et al* (79) demonstrated that promoter methylation of the BMP2 gene in the breast cancer cell line MCF-7 downregulates BMP2 expression, enhancing drug resistance and promoting cancer progression. Conversely, other studies have revealed that treating the human and mouse breast cancer cell, MCF-7, with BMP2 inhibits cell migration and proliferation, revealing its anti-cancer effects (80,81).

In nasopharyngeal carcinoma, the BMP2 promoter enhances its expression by binding to SOX9, thereby activating the BMP2-induced mTOR signaling pathway and promoting the proliferation, migration and invasion of nasopharyngeal carcinoma cells (77,82). Research reveals that BMP2 suppresses gastric cancer cell proliferation by arresting the cell cycle via a non-SMAD BMP pathway that downregulates EZH2 (83), consistent with the findings of the present study. The present study indicates that DAP induces the upregulation of BMP2 expression, which subsequently influences cell proliferation. This effect may be attributed to the ability of BMP2 upregulation to activate AMPK, leading to the inhibition of the mTOR signaling pathway. Specifically, the activation of AMPK suppresses the activity of the mTORC1 complex via phosphorylation, thereby disrupting protein synthesis and metabolic processes essential for cell proliferation (84).

The limited number of DEGs identified at 24 h post-treatment suggests an early drug response phase rather than transcriptomic reprogramming. Similar results were seen in other studies: Only 357 and 455 DEGs were found in two sweet corn varieties under low-temperature stress (85) and 551 DEGs were detected after vascular hepatocyte differentiation in pigs (86). The limited number of DEGs observed in this study may be attributed to three potential factors: Inadequate drug exposure or low concentrations preventing a significant transcriptional response, cellular heterogeneity causing varied drug sensitivities and diluting signals, and the phenotypic lag effect (87) where drugs act through early gene activity and protein interactions. Future work will assess DAP's effects on cervical cancer HeLa cells by extending treatment time and testing more concentration levels.

Following DAP treatment, cells exhibited signs of apoptosis. Transcriptome analysis and RT-qPCR validation confirmed that this apoptotic response was associated with the upregulation of three genes: TGIF2, ID1 and BMP2. This finding raises the question of whether DAP interacts directly with the corresponding proteins encoded by these genes. To investigate potential protein-level interactions between DAP and the TGIF2, ID1 and BMP2 proteins, the present study employed molecular docking technology to evaluate their binding affinities. Molecular docking is based on the lock-and-key principle, examining how the spatial structure and electrostatic characteristics of small molecules match the active sites of their target proteins. The lower the binding energy between a small molecule and its target protein, the stronger their interaction. Typically, a binding energy <-4.25 kcal/mol indicates some degree of binding activity; <-5.0 kcal/mol suggests good binding activity; and <-7.0 kcal/mol indicates strong binding activity (88).

While this study elucidated the potential binding modes of DAP with TGIF2, ID1 and BMP2 proteins using molecular docking, it is important to acknowledge the intrinsic limitations of static docking models. Molecular docking generally relies on rigid or semi-flexible receptor models, which may fail to adequately capture the conformational dynamics of protein-ligand complexes under physiological conditions (89). To address these limitations, the present study incorporated MD simulations for dynamic validation. To further elucidate the molecular interactions underlying the anticancer potential of DAP, MD simulations were carried out to evaluate its binding stability with key regulatory proteins involved in cervical cancer progression. The simulations analyzed ligand-protein interactions with TGIF2, ID1 and BMP2 over a 200-nanosecond trajectory. RMSD analysis revealed that all three complexes exhibited initial structural fluctuations before achieving stable conformations, suggesting successful ligand binding. Similarly, RMSF analysis identified key residues exhibiting flexibility within each protein-ligand complex, further supporting their dynamic interactions. These computational findings provide valuable insights into the structural basis of the biological activity of DAP, reinforcing its potential as a novel therapeutic candidate for cervical cancer.

The present study provides insights into the inhibitory mechanisms of DAP on cervical cancer cells but is limited by using only the HeLa cell line. Initial screening (Table SII) revealed DAP has notable activity against HeLa and SiHa cells, however, only 11.9 mg of purified DAP was available. Due to this limitation, mechanistic studies focused on HeLa cells. Using a single cell line restricts the generalizability of the findings, as cervical cancer is heterogeneous and responses vary across cell lines. Thus, results obtained with HeLa cells may not fully represent other subtypes. The proposed mechanisms require further validation for broader applicability.

Future work will validate key experiments in additional cell lines such as CaSki and SiHa and, where feasible, use patient-derived cells or organoids for clinically relevant models. Simultaneously, this study will establish subcutaneous xenograft cervical cancer models in immunodeficient nude mice through the injection of cervical cancer cells. DAP will be administered subcutaneously at low, medium and high doses to these models. This study will utilize the untreated models as the control group, and paclitaxel-treated models as the positive control. *In vivo* experiments will evaluate the efficacy of DAP by analyzing tumor growth, final tumor size, pathological changes and marker protein expression across all groups. Acute or subchronic toxicity studies using healthy mice will assess behavioral changes, body weight, food/water intake, blood profiles, biochemical parameters and organ histopathology (liver, kidney, spleen, lung, heart and intestine). These analyses will aim to identify toxic target organs, determine the maximum tolerated dose and establish a safety margin. Together, these experiments will provide preclinical data to assess the clinical potential of DAP and guide its development as a therapy.

Collectively, a novel endophytic fungal species, *Alternaria semiverrucosa*, was isolated from *Taxus chinensis* var. *marei* collected in Guiyang, China. DAP was subsequently obtained from the fermentation metabolites of *Alternaria semiverrucosa*. The inhibitory effects of DAP on cervical cancer HeLa cells suggest that it exhibits high efficacy and low toxicity, making it a promising candidate for further investigation, and warranting further investigation into its underlying molecular mechanisms and therapeutic potential. Future studies integrating experimental validation of these molecular interactions will be key to confirming efficacy and clinical applicability of DAP.

Acknowledgements

The authors would like to thank Dr Heng Luo for their assistance and guidance with the *in vitro* experiments which were conducted at the Key Laboratory of Chemistry for Natural Products of Guizhou Province, Chinese Academy of Sciences, Guiyang, China. The authors would also like to thank Guiyang Stomatological Hospital (Guiyang, China) for donating HGF-1 human gingival fibroblasts.

Funding

The present study was supported by the National Natural Science Foundation of China (grant nos. 32460007, 32170019 and 31670027).

Availability of data and materials

The data generated in the present study may be found in the National Center for Biotechnology Information under accession number PRJNA1272013, or at the following URL: https://www.ncbi.nlm.nih.gov/bioproject/PRJNA1272013/.

Authors' contributions

JK and MY conceptualized the present study. MY and YL developed the methodology. LH and ZH were responsible for the application and implementation of the Molecular dynamics simulation software. MY, YL and JK conducted the analysis of the experimental data. MY, YL and ZH carried out cell validation experiments. ZH and YL managed the transcriptome data curation and analysis. MY and LH wrote the original draft. JK, MY and YL contributed to reviewing and editing. LH, ZH and YL handled the microscopy images. JK supervised the project and administered it. MY, YL, ZH and JK confirm the authenticity of all the raw data. All authors have read and agreed to the published version of the manuscript.

Ethics approval and consent to participate

Not applicable.

Patient consent for publication

Not applicable.

Competing interests

The authors declare that they have no competing interests.

References

1. Cohen PA, Jhingran A, Oaknin A and Denny L: Cervical cancer. Lancet 393: 169-182, 2019.
2. Kokhdan EP, Khodavandi P, Ataeyan MH, Alizadeh F, Khodavandi A and Zaheri A: Anti-cancer activity of secreted aspartyl proteinase protein from Candida tropicalis on human cervical cancer HeLa cells. Toxicon 249: 108073, 2024.
3. Bray F, Jemal A, Soerjomataram I, Siegel RL, Ferlay J, Sung H and Laversanne M: Global cancer statistics 2022: Globocan estimates of incidence and mortality worldwide for 36 cancers in 185 countries. CA Cancer J Clin 74: 229-263, 2024.
4. Luan H: Human papilloma virus infection and its associated risk for cervical lesions: A cross-sectional study in Putuo area of Shanghai, China. BMC Womens Health 23: 28, 2023.
5. Wang R, Pan W, Jin L, Huang W, Li Y, Wu D, Gao C, Ma D and Liao S: Human papillomavirus vaccine against cervical cancer: Opportunity and challenge. Cancer Lett 471: 88-102, 2020.
6. Xu J, Tan ZC, Shen ZY, Shen XJ and Tang SM: Cordyceps cicadae polysaccharides inhibit human cervical cancer hela cells proliferation via apoptosis and cell cycle arrest. Food Chem Toxicol 148: 111971, 2021.
7. Zhang X, Song Z, Li Y, Wang H, Zhang S, Reid AM, Lall N, Zhang J, Wang C, Lee D, *et al*: Cytotoxic and antiangiogenetic xanthones inhibiting tumor proliferation and metastasis from *garcinia xipshuanbannaensis*. J Nat Prod 84: 1515-1523, 2021.
8. Kusari S, Hertweck C and Spiteller M: Chemical ecology of endophytic fungi: Origins of secondary metabolites. Chem Biol 19: 792-798, 2012.
9. Zhang HW, Song YC and Tan RX: Biology and chemistry of endophytes. Nat Prod Rep 23: 753-771, 2006.

10. Bashyal BP, Wijeratne EM, Tillotson J, Arnold AE, Chapman E and Gunatilaka AA: Chlorinated dehydrocurvularins and alterperylenepoxide A from Alternaria sp. AST0039, a fungal endophyte of Astragalus lentiginosus. J Nat Prod 80: 427-433, 2017.
11. Li SJ, Zhang X, Wang XH and Zhao CQ: Novel natural compounds from endophytic fungi with anticancer activity. Eur J Med Chem 156: 316-343, 2018.
12. Zhu M, Zhang X, Feng H, Dai J, Li J, Che Q, Gu Q, Zhu T and Li D: Penicisulfuranols A-F, alkaloids from the mangrove endophytic fungus Penicillium janthinellum HDN13-309. J Nat Prod 80: 71-75, 2017.
13. Chakravarthi BV, Sujay R, Kuriakose GC, Karande AA and Jayabaskaran C: Inhibition of cancer cell proliferation and apoptosis-inducing activity of fungal taxol and its precursor baccatin III purified from endophytic *Fusarium solani*. Cancer Cell Int 13: 105, 2013.
14. Wu LS, Hu CL, Han T, Zheng CJ, Ma XQ, Rahman K and Qin LP: Cytotoxic metabolites from Perenniporia tephropora, an endophytic fungus from Taxus chinensis var. mairei. Appl Microbiol Biotechnol 97: 305-315, 2013.
15. Uzor PF, Ebrahim W, Osadebe PO, Nwodo JN, Okoye FB, Müller WE, Lin W, Liu Z and Proksch P: Metabolites from Combretum dolichopetalum and its associated endophytic fungus Nigrospora oryzae--evidence for a metabolic partnership. Fitoterapia 105: 147-150, 2015.
16. Wani MC, Taylor HL, Wall ME, Coggon P and McPhail AT: Plant antitumor agents. VI. The isolation and structure of taxol, a novel antileukemic and antitumor agent from Taxus brevifolia. J Am Chem Soc 93: 2325-2327. 1971.
17. Zaiyou J, Li M, Xu G and Zhou X: Isolation of an endophytic fungus producing baccatin III from Taxus wallichiana var. mairei. J Ind Microbiol Biotechnol 40: 1297-1302, 2013.
18. Zaiyou J, Li M and Xiqiao H: An endophytic fungus efficiently producing paclitaxel isolated from Taxus wallichiana var. mairei. Medicine (Baltimore) 96: e7406, 2017,
19. Fan ZY, PengJ, Lou JQ, Chen Y, Wu XM, Tan R and Tan RX: Neuroprotective α-pyrones from Nigrospora oryzae, an endophytic fungus residing in Taxus chinensis var. mairei. Phytochemistry 216: 113873, 2023.
20. Hu D, Fan Y, Tan Y, Tian Y, Liu N, Wang L, Zhao D, Wang C and Wu A: Metabolic profiling on alternaria toxins and components of Xinjiang Jujubes incubated with pathogenic alternaria Alternata and Alternaria tenuissima via orbitrap high-resolution mass spectrometry. J Agri Food Chem 65: 8466-8474, 2017.
21. Andersen B, Nielsen KF, Fernández Pinto V and Patriarca A: Characterization of Alternaria strains from Argentinean blueberry, tomato, walnut and wheat. Int J Food Microbiol 196: 1-10, 2015.
22. Yang CL, Wu HM, Liu CL, Zhang X, Guo ZK, Chen Y, Liu F, Liang Y, Jiao RH, Tan RX and Ge HM: Bialternacins A-F, aromatic polyketide dimers from an endophytic Alternaria sp. J Nat Prod 82: 792-797, 2019.
23. Xi J, Tian LL, Xi J, Girimpuhwe D, Huang C, Ma R, Yao X, Shi D, Bai Z, Wu QX and Fang J: Alterperylenol as a novel thioredoxin reductase inhibitor induces liver cancer cell apoptosis and ferroptosis. J Agric Food Chem 70: 15763-15775, 2022.
24. Li L, Yang M, Yu J, Cheng S, Ahmad M, Wu C, Wan X, Xu B, Ben-David Y and Luo H: A novel L-phenylalanine dipeptide inhibits the growth and metastasis of prostate cancer cells via targeting DUSP1 and TNFSF9. Int J Mol Sci 23: 10916, 2022.
25. Liu Y, Xin ZZ, Song J, Zhu XY, Liu QN, Zhang DZ, Tang BP, Zhou CL and Dai LS: Transcriptome analysis reveals potential antioxidant defense mechanisms in Antheraea pernyi in response to zinc stress. J Agric Food Chem 66: 8132-8141, 2018.
26. Chen C, Chen H, Zhang Y, Thomas HR, Frank MH, He Y and Xia R: TBtools: An integrative toolkit developed for interactive analyses of big biological data. Mol Plant 13: 1194-1202, 2020.
27. Livak KJ and Schmittgen TD: Analysis of relative gene expression data using real-time quantitative PCR and the 2(-Delta Delta C(T)) method. Methods 25: 402-408, 2001.
28. Case DA, Aktulga HM, Belfon K, Cerutti DS, Cisneros GA, Cruzeiro VWD, Forouzesh N, Giese TJ, Götz AW, Gohlke H, *et al*: Amber Tools. J Chem Inf Model 63: 6183-6191, 2023.
29. Shaw DE, Maragakis P, Lindorff-Larsen K, Piana S, Dror RO, Eastwood MP, Bank JA, Jumper JM, Salmon JK, Shan Y and Wriggers W: Atomic-level characterization of the structural dynamics of proteins. Science 330: 341-346, 2010.
30. Tian C, Kasavajhala K, Belfon KAA, Raguette L, Huang H, Migues AN, Bickel J, Wang Y, Pincay J, Wu Q and Simmerling C: ff19SB: Amino-acid-specific protein backbone parameters trained against quantum mechanics energy surfaces in solution. J Chem Theory Comput 16: 528-552, 2020.
31. Izadi S, Anandakrishnan R and Onufriev AV: Building water models: A different approach. J Phys Chem Lett 5: 3863-3871, 2014.
32. Wang H, Gao X and Fang J: Multiple staggered mesh ewald: Boosting the accuracy of the smooth particle mesh ewald method. J Chem Theory Comput 12: 5596-5608, 2016.
33. Donnelly SM, Lopez NA and Dodin IY: Steepest-descent algorithm for simulating plasma-wave caustics via metaplectic geometrical optics. Phys Rev E 104: 025304, 2021.
34. Bussi G, Donadio D and Parrinello M: Canonical sampling through velocity rescaling. J Chem Phys 126: 014101, 2007.
35. Nosé S and Klein ML: Constant pressure molecular dynamics for molecular systems. Mol Phys 50: 1055-1076, 1983.
36. Zhang SY, Li ZL, Bai J, Wang Y, Zhang LM, Wu X and Hua HM: A new perylenequinone from a halotolerant fungus, Alternaria sp. M6. Chin J Nat Med 10: 68-71, 2012.
37. Campos FR, Barison A, Daolio C, Ferreira AG and Rodrigues-Fo E: Complete 1H and 13C NMR assignments of aurasperone A and fonsecinone A, two bis-naphthopyrones produced by Aspergillus aculeatus. Magn Reson Chem 43: 962-965, 2005.
38. Xiong HY, Fei DQ, Zhou JS, Yang CJ and Ma GL: Steroids and other constituents from the mushroom Armillaria lueo-virens. Chem Nat Compd 45: 759-761, 2009.
39. Wu J, Choi JH, Yoshida M, Hirai H, Harada E, Masuda K, Koyama T, Yazawa K, Noguchi K, Nagasawa K and Kawagishi H: Osteoclast-forming suppressing compounds, gargalols A, B, and C, from the edible mushroom Grifola gargal. Tetrahedron 67: 6576-6581, 2011.
40. Yue JM, Chen SN, Lin ZW and Sun HD: Sterols from the fungus lactarium volemus. Phytochemistry 56: 801-806, 2001.
41. Ding T, Zhou Y, Qin JJ, Yang LJ, Zhang WD and Shen YH: Chemical constituents from wetland soil fungus penicillium oxalicum GY1. Fitoterapia 142: 104530, 2020.
42. Liu S, Sun C, Ha Y, Ma M, Wang N, Zhou Y and Zhang Z: Novel antibacterial alkaloids from the mariana trench-derived actinomycete streptomyces sp. SY2255.Tetrahedron Lett 137: 154935, 2024.
43. Wu B, Lin WH, Gao HY, Zheng L, Wu LJ and Kim CS: Four new antibacterial constituents from Senecio cannabifolius. Pharm Biol 44: 440-444, 2006.
44. Pitera JW: Expected distributions of root-mean-square positional deviations in proteins. J Phys Chem B 118: 6526-6530, 2014.
45. Trott O and Olson AJ: AutoDock vina: Improving the speed and accuracy of docking with a new scoring function, efficient optimization, and multithreading. J Comput Chem 31: 455-461, 2010.
46. Fu Y, Wu F, Huang JH, Chen YC and Luo MB: Simulation study on the extension of semi-flexible polymer chains in cylindrical channel. Chin J Polym Sci 37:1053-1060, 2019.
47. Cao X, Hummel MH, Wang Y, Simmerling C and Coutsias EA: Exact analytical algorithm for the solvent-accessible surface area and derivatives in implicit solvent molecular simulations on GPUs. J Chem Theory Comput 20: 4456-4468, 2024.
48. Wang Y and Wang Y: HBCalculator: A tool for hydrogen bond distribution calculations in molecular dynamics simulations. J Chem Inf Model 64: 1772-1777, 2024.
49. Jiang D, Du H, Zhao H, Deng Y, Wu Z, Wang J, Zeng Y, Zhang H, Wang X, Wang E, *et al*: Assessing the performance of MM/PBSA and MM/GBSA methods. 10. Prediction reliability of binding affinities and binding poses for RNA-ligand complexes. Phys Chem Chem Phys 26: 10323-10335, 2024.
50. Liao Q: Enhanced sampling and free energy calculations for protein simulations. Prog Mol Biol Transl Sci 170: 177-213, 2020.
51. Bai F, Xu Y, Chen J, Liu Q, Gu J, Wang X, Ma J, Li H, Onuchic JN and Jiang H: Free energy landscape for the binding process of Huperzine A to acetylcholinesterase. Proc Natl Acad Sci USA 110: 4273-4278, 2013.
52. Zhang Z, Liu M, An Y, Gao C, Wang T, Zhang Z, Zhang G, Li S, Li W, Li M and Wang G: Targeting immune microenvironment in cervical cancer: Current research and advances. J Transl Med 23: 888, 2025.
53. Sharma S, Deep A and Sharma AK: Current treatment for cervical cancer: An update. Anticancer Agents Med Chem 20: 1768-1779, 2020.

54. Barra F, Lorusso D, Leone Roberti Maggiore U, Ditto A, Bogani G, Raspagliesi F and Ferrero S: Investigational drugs for the treatment of cervical cancer. Expert Opin Investig Drugs 26: 389-402, 2017.
55. Giudice E, Mirza MR and Lorusso D: Advances in the management of recurrent cervical cancer: State of the art and future perspectives. Curr Oncol Rep 25: 1307-1326, 2023.
56. Newman DJ and Giddings LA: Natural products as leads to antitumor drugs. Phytochem Rev 13:123-137, 2014.
57. Baek SH: Editorial for the special issue 'Anticancer activity and metabolic pathways of natural products 2.0'. Biomedicines 13: 2083, 2025.
58. Pero RW, Posner H, Blois M, Harvan D and Spalding JW: Toxicity of metabolites produced by the 'Alternaria'. Environ Health Perspect 4: 87-94, 1973
59. Fang ZF, Yu SS, Zhou WQ, Chen XG, Ma SG, Li Y and Qu J: A new isocoumarin from metabolites of the endophytic fungus *Alternaria tenuissima* (Nees & T. Nees: Fr.) Wiltshire. Chinese Chem Lett 23: 317-320, 2012.
60. Ma Y, Lin Q, Yang Y, Liang W, Salamone SJ, Li Y, Lin Y, Zhao H, Zhao Y, Fang W, *et al*: Clinical pharmacokinetics and drug exposure-toxicity correlation study of docetaxel based chemotherapy in Chinese head and neck cancer patients. Ann Transl Med 8: 236, 2020.
61. Yang Z, Liu Z, Ablise M, Jia J, Maimaiti A, Lv ZY, Mutalipu Z, Yan T, Wang Y, Aihaiti A, *et al*: Design, synthesis, and in vitro and in vivo anti-drug resistant cervical cancer activity of novel licochalcone A derivatives based on dual targeting of VEGFR-2/P-gp. Bioorg Chem 163: 108639, 2025.
62. Zafar A, Khatoon S, Khan MJ, Abu J and Naeem A: Advancements and limitations in traditional anti-cancer therapies: A comprehensive review of surgery, chemotherapy, radiation therapy, and hormonal therapy. Discov Oncol 16: 607, 2025.
63. Raman R, Debata S, Govindarajan T and Kumar P: Targeting triple-negative breast cancer: Resistance mechanisms and therapeutic advancements. Cancer Med 14: e70803, 2025.
64. Li W, Xu F, Shuai W, Sun H, Yao H, Ma C, Xu S, Yao H, Zhu Z, Yang DH, *et al*: Discovery of novel quinoline-chalcone derivatives as potent antitumor agents with microtubule polymerization inhibitory activity. J Med Chem 62: 993-1013, 2019.
65. França GS, Baron M, King BR, Bossowski JP, Bjornberg A, Pour M, Rao A, Patel AS, Misirlioglu S, Barkley D, *et al*: Cellular adaptation to cancer therapy along a resistance continuum. Nature 631: 876-883, 2024.
66. Pang L, Cheng Y, Zou S and Song J: Long noncoding RNA SNHG7 contributes to cell proliferation, migration, invasion and epithelial to mesenchymal transition in non-small cell lung cancer by regulating miR-449a/TGIF2 axis. Thorac Cancer 11: 264-276, 2020.
67. Liu K, Zhang Y, Liu L and Yuan Q: *MALAT1* promotes proliferation, migration, and invasion of MG63 cells by upregulation of *TGIF2* via negatively regulating *miR-129*. Onco Targets Ther 11: 8729-8740, 2018.
68. Xi L, Zhang Y, Kong S and Liang W: *miR-34* inhibits growth and promotes apoptosis of osteosarcoma in nude mice through targetly regulating TGIF2 expression. Biosci Rep 38: BSR20180078, 2018.
69. Weiler S, Ademokun JA and Norton JD: ID helix-loop-helix proteins as determinants of cell survival in B-cell chronic lymphocytic leukemia cells in vitro. Mol Cancer 14: 30, 2015.
70. Ruzinova MB and Benezra R: Id proteins in development, cell cycle and cancer. Trends Cell Biol 13: 410-418, 2003.
71. Ouyang XS, Wang X, Ling MT, Wong HL, Tsao SW and Wong YC: Id-1 stimu-lates serum independent prostate cancer cell proliferation through inactivation of p16(INK4a)/pRB pathway. Carcinogenesis 23: 721-725, 2002.
72. Ling MT, Wang X, Ouyang XS, Lee TK, Fan TY, Xu K, Tsao SW and Wong YC: Activation of MAPK signaling pathway is essential for Id-1 induced serum independent prostate cancer cell growth. Oncogene 21: 8498-8505, 2002.
73. Su Y, Zheng L, Wang Q, Bao J, Cai Z and Liu A: The PI3K/Akt pathway upregulates Id1 and integrin α4 to enhance recruitment of human ovarian cancer endothelial progenitor cells. BMC Cancer 10: 459, 2010.
74. Sun WZ, Li MH, Chu M, Wei LL, Bi MY, He Y and Yu LB: Id1 knockdown induces the apoptosis and inhibits the proliferation and invasion of ovarian cancer cells. Eur Rev Med Pharmacol Sci 20: 2812-2818, 2016.
75. Papaspyridonos M, Matei I, Huang Y, do Rosario Andre M, Brazier-Mitouart H, Waite JC, Chan AS, Kalter J, Ramos I, Wu Q, *et al*: Id1 suppresses anti-tumour immune responses and promotes tumour progression by impairing myeloid cell maturation. Nat Commun 6: 6840, 2015.
76. Wang MH, Zhou XM, Zhang MY, Shi L, Xiao RW, Zeng LS, Yang XZ, Zheng XFS, Wang HY and Mai SJ: BMP2 promotes proliferation and invasion of nasopharyngeal carcinoma cells via mTORC1 pathway. Aging (Albany NY) 9: 1326-1340, 2017.
77. Lan L, Evan T, Li H, Hussain A, Ruiz EJ, Zaw Thin M, Ferreira RMM, Ps H, Riising EM, Zen Y, *et al*: GREM1 is required to maintain cellular heterogeneity in pancreatic cancer. Nature 607: 163-168, 2022.
78. Huang S, Wang Y, Luo L, Li X, Jin X, Li S, Yu X, Yang M and Guo Z: BMP2 is related to Hirschsprung's disease and required for enteric nervous system development. Front Cell Neurosci 13: 523, 2019.
79. Du M, Su XM, Zhang T and Xing YJ: Aberrant promoter DNA methylation inhibits bone morphogenetic protein 2 expression and contributes to drug resistance in breast cancer. Mol Med Rep 10: 1051-1055, 2014.
80. Waite KA and Eng C: BMP2 exposure results in decreased PTEN protein degradation and increased PTEN levels. Hum Mol Genet 12: 679-684, 2003.
81. Buijs JT, van der Horst G, van den Hoogen C, Cheung H, de Rooij B, Kroon J, Petersen M, van Overveld PG, Pelger RC and van der Pluijm G: The BMP2/7 heterodimer inhibits the human breast cancer stem cell subpopulation and bone metastases formation. Oncogene 31: 2164-2174, 2012.
82. Xiao B, Zhang W, Kuang Z, Lu J, Li W, Deng C, He Y, Lei T, Hao W, Sun Z and Li L: SOX9 promotes nasopharyngeal carcinoma cell proliferation, migration and invasion through BMP2 and mTOR signaling. Gene 715: 144017, 2019.
83. Chen Z, Yuan L, Li X, Yu J and Xu Z: BMP2 inhibits cell proliferation by downregulating EZH2 in gastric cancer. Cell Cycle 21: 2298-2308, 2022.
84. Vora M, Mondal A, Jia D, Gaddipati P, Akel M, Gilleran J, Roberge J, Rongo C and Langenfeld J: Bone morphogenetic protein signaling regulation of AMPK and PI3K in lung cancer cells and C. elegans. Cell Biosci 12: 76, 2022.
85. Mao J, Yu Y, Yang J, Li G, Li C, Qi X, Wen T and Hu J: Comparative transcriptome analysis of sweet corn seedlings under low-temperature stress. Crop J 5: 396-406, 2017.
86. Chen L, Zhang Y, Chen H, Zhang X, Liu X, He Z, Cong P, Chen Y and Mo D: Comparative transcriptome analysis reveals a more complicated adipogenic process in intramuscular stem cells than that of subcutaneous vascular stem cells. J Agric Food Chem 67: 4700-4708, 2019.
87. Zhao W, Li J, Chen MM, Luo Y, Ju Z, Nesser NK, Johnson-Camacho K, Boniface CT, Lawrence Y, Pande NT, *et al*: Large-scale characterization of drug responses of clinically relevant proteins in cancer cell lines. Cancer Cell 38: 829-843.e4, 2020.
88. Istyastono EP, Radifar M, Yuniarti N, Prasasty VD and Mungkasi S: PyPLIF HIPPOS: A molecular interaction fingerprinting tool for docking results of autoDock vina and PLANTS. J Chem Inf Model 60: 3697-3702, 2020.
89. Errington D, Schneider C, Bouysset C and Dreyer FA: Assessing interaction recovery of predicted protein-ligand poses. J Cheminform 17: 76, 2025.
90. Wang L, Zhang J, Zhang W, Zheng M, Guo H, Pan X, Li W, Yang B and Ding L: The inhibitory effect of adenosine on tumor adaptive immunity and intervention strategies. Acta Pharm Sin B 14: 1951-1964, 2024.